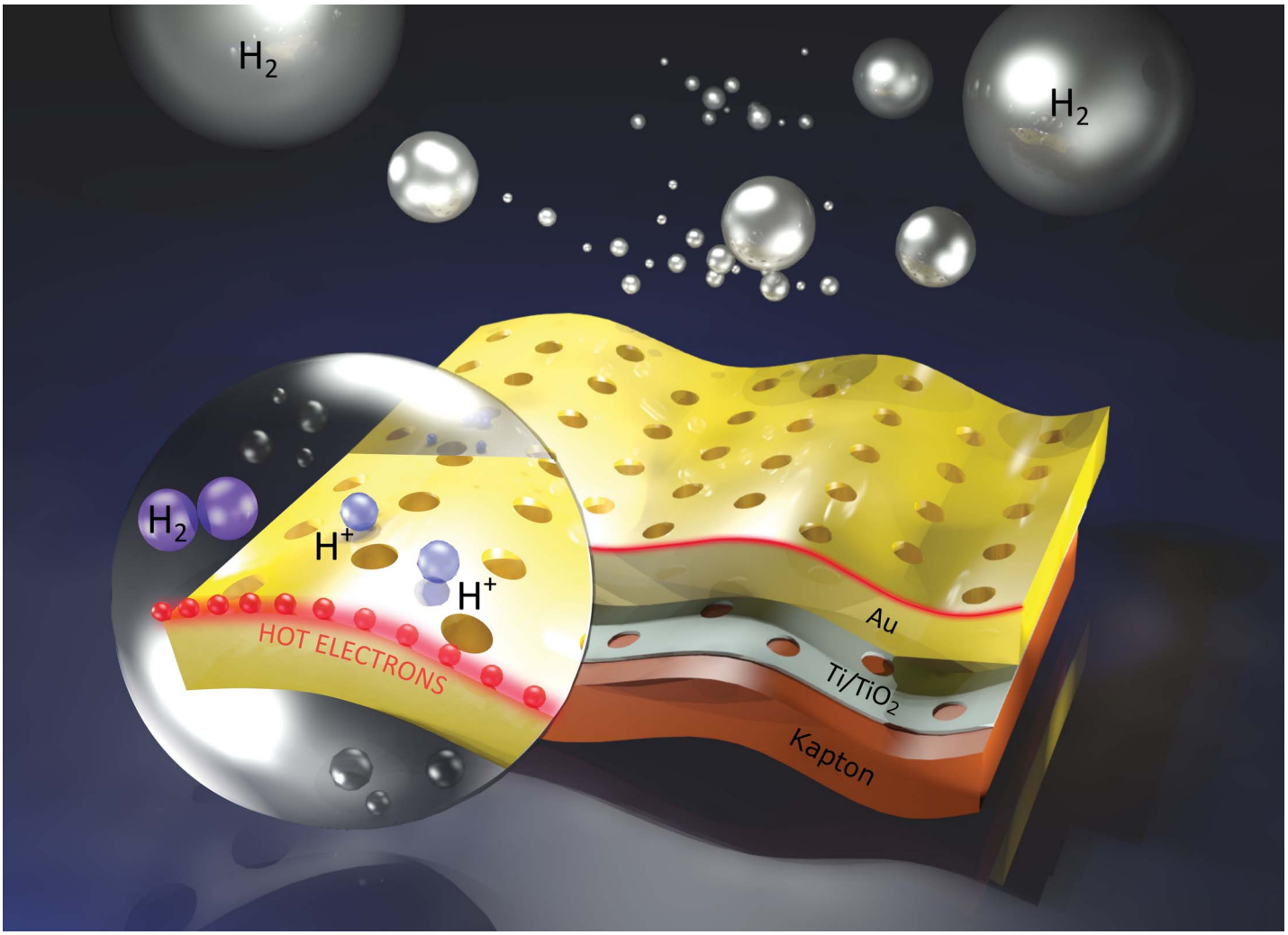

Showcasing joint research of the team lead by Professor Szunerits in France, University of Lille, and colleagues in Belgium, at KU Leuven and UCLouvain, Professor Melinte.

Enhanced electrocatalytic hydrogen evolution on a plasmonic electrode: the importance of the Ti/TiO_2 adhesion layer

Ultra-thin gold layers patterned on mechanically flexible polyimide layers for plasmonic photocatalysis step up hydrogen evolution reaction via the generation and unique dynamics of hot electrons.

As featured in:

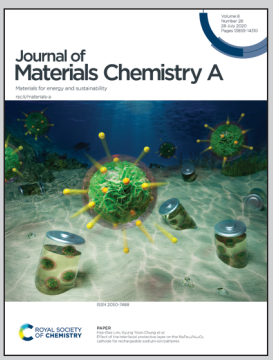

See Sabine Szunerits *et al.*, *J. Mater. Chem. A*, 2020, **8**, 13980.

ROYAL SOCIETY OF CHEMISTRY

rsc.li/materials-a

Registered charity number: 207890

Journal of Materials Chemistry A

ROYAL SOCIETY OF CHEMISTRY

PAPER

Cite this: *J. Mater. Chem. A*, 2020, **8**, 13980

Enhanced electrocatalytic hydrogen evolution on a plasmonic electrode: the importance of the Ti/TiO_2 adhesion layer†

Liuqing Pang,[a] Alexandre Barras,[a] Vladyslav Mishyn,[a] Georgiana Sandu,[b] Sorin Melinte,[b] Palaniappan Subramanian,[c] Rabah Boukherroub[a] and Sabine Szunerits *[a]

Received 28th February 2020
Accepted 27th April 2020

DOI: 10.1039/d0ta02353a

rsc.li/materials-a

The electrochemical production of hydrogen is enjoying renewed vigor due to its great promise as an environmentally friendly energy alternative. Herein, we demonstrate the capacity of nanoperforated gold films deposited on flexible substrates coated with nanometer thick Ti/TiO_2 adhesion layers for electrochemical water splitting under light irradiation. The strong plasmonic induced electromagnetic field enhancement, which occurs under the illumination of plasmonic electrodes, facilitates the dissociation of water into hydrogen and improves the electrocatalytic hydrogen evolution activity beyond that of platinum. Under illumination at 980 nm at 2 W cm^{-2}, a current density of -10 mA cm^{-2} was recorded at a low overpotential of $\eta \approx -0.045$ V (*vs.* RHE); under the same conditions, a Pt electrode achieved -10 mA cm^{-2} at $\eta \approx -0.048$ V (*vs.* RHE). Mechanistic investigations revealed that plasmon-excited perforated gold thin layers are an efficient source of hot electrons, contributing to their injection into the underlying TiO_2-based adhesion layer. Direct electrochemical reduction of water appears to be a parallel reaction pathway to sustain the hydrogen evolution reaction on the interface. Both reaction pathways decrease the activation energy for the hydrogen evolution reaction similar to the benchmark Pt electrocatalyst.

1. Introduction

Identification of efficient electrocatalysts other than platinum for the hydrogen evolution reaction (HER) is timely and represents a growing field of research and development. The clean and potentially cost-effective pathway for hydrogen (H_2) production *via* electro-reductive water splitting makes H_2 the ultimate fuel of the future.[1,2] The energy required to drive the reductive water-splitting reaction ($4H^+ + 4e^- \rightarrow 2H_2(g)$) necessitates the use of catalysts, with platinum being at present the most active catalyst for the HER in acidic solutions.[3,4] Polished polycrystalline Pt or platinized electrodes can achieve -10 mA cm^{-2} at an overpotential of $\eta \approx -0.040$ V.[5] The large scale application of Pt catalysts is yet limited by their high cost and low abundance, motivating researchers to discover cost-effective alternatives achieving -10 mA cm^{-2} at $\eta \approx -0.100$ V. Yet, only some catalysts such as electrodeposited NiMo and NiMoCo films,[4] amorphous molybdenum sulphide films deposited on F-doped tin oxide (FTO) electrodes,[6] and ternary pyrite-type cobalt phosphosulphide (CoPS)[7] showed comparable activities attaining -10 mA cm^{-2} at $\eta \approx -0.050$ V,[4] -15 mA cm^{-2} at $\eta = -0.200$ V,[6] and -10 mA cm^{-2} at $\eta = -0.048$ V,[7] respectively. The search for electrocatalytic systems with efficiencies comparable to or even better than that of platinum remains a demanding task up to now. Nanoporous graphene with single-atom nickel dopants was proposed by Qiu *et al.* and it achieved a current density of -10 mA cm^{-2} at $\eta = -0.050$ V in 0.5 M H_2SO_4 with excellent cycling stability.[8] Tan *et al.* demonstrated the potential of 3D nanoporous cobalt phosphide (np-Co_2P) with a pore size of 30 nm for the HER with a current density of -10 mA cm^{-2} at $\eta = -0.080$ V.[9]

Although substantial progress has been made in this field, the search for HER catalysts is focused mainly only on designing platinum-free electrocatalysts, neglecting the integration of other driving sources, especially plasmonic phenomena.[10–19] Plasmonic enhancement is mainly achieved through three mechanisms, namely, far-field scattering, near-field enhancement and charge carrier or resonant energy transfer.[20] While plasmon-enhanced photocatalytic water splitting has been demonstrated by several research groups,[10,12,21–23] plasmon-mediated electrochemical water reduction has been

[a]*Univ. Lille, CNRS, Centrale Lille, ISEN, Univ. Valenciennes, UMR 8520 – IEMN, F-59000 Lille, France. E-mail: sabine.szunerits@univ-lille.fr*

[b]*Institute of Information and Communication Technologies, Electronics and Applied Mathematics, Université Catholique de Louvain, 1348 Louvain-la-Neuve, Belgium*

[c]*Department of Materials Engineering, KU Leuven, Kateelpark Arenberg, Heverlee – 3001, Belgium*

† Electronic supplementary information (ESI) available. See DOI: 10.1039/d0ta02353a

This journal is © The Royal Society of Chemistry 2020

described only in a few reports.[24–30] These studies were mainly based on the coupling of plasmonic nanostructures with few-layered MoS_2 materials due to the excellent catalytic activity of MoS_2 for the HER.[11,28–31] The work of Shi *et al.* was based on drop-coating of Au nanorods/MoS_2 nanosheet hybrids onto glassy carbon electrodes, reaching a current density of -10 mA cm^{-2} at $\eta = -0.120$ V.[11] The catalytic enhancement was attributed to an increase in carrier density in MoS_2 induced by the injection of hot electrons of the plasmonic nanostructures. Wang *et al.* reported recently the possibility of boosting electrocatalytic hydrogen evolution over metal–organic frameworks by plasmon-induced hot-electron injection *via* gold nanorods.[26] Upon irradiation with an 808 nm laser, a current density of -10 mA cm^{-2} was recorded at an overpotential of $\eta = -0.135$ V.

We report here on plasmon-accelerated electrocatalytic reduction of water in acid solution and H_2 production on different plasmonic electrodes. These systems comprise several of the essential components for boosting the electrocatalytic HER: (i) a plasmonic resonant structure in the form of Au NH layers with excellent subwavelength light manipulation properties and electromagnetic field enhancement; (ii) an electrical interface working as a heterogeneous electrocatalyst for water reduction; and in one case, (iii) a Ti/TiO_2 adhesion layer forming a Mott–Schottky barrier with the nanopatterned gold layer.

We show that under laser illumination at 980 nm (2 W cm^{-2}) on an interface comprising a thin Ti/TiO_2 layer next to the Au NHs (denoted as S2 in this work), enabling the injection of formed hot electrons from the plasmonic interface to absorbed water molecules, a current density of -10 mA cm^{-2} can be attained at an overpotential of $\eta \approx -0.045$ V. The HER activity of commercial benchmark Pt was not affected by laser illumination and achieved -10 mA cm^{-2} at -0.048 V *vs.* RHE.

2. Results and discussion

2.1 Nanoperforated gold thin film electrodes

The tunable optical properties of gold nanostructures and their good electrical conductivity make noble metal ordered architectures ideally suited for the construction of plasmonic electrodes.[32,33] Colloidal lithography was adopted to generate different types of nanostructured electrodes on Kapton (K) (Fig. 1).

The samples are structured and labelled as follows: (S1) K/Au NHs (50 nm), (S2) K/Ti/TiO_2/Au NHs (50 nm), and (S3) K/Ti/TiO_2 (30 nm). Ultra-thin (<3 nm), disordered adhesion layers of Ti obtained by physical vapor deposition, as those used here, typically display a metal–insulator transition and contain amorphous TiO_2.[34] Note that when titanium is exposed to air, a native TiO_2 layer is formed spontaneously. The electron microscopy images of the specimens are displayed in Fig. S1a,† revealing the characteristics of nanoperforated thin film metallic structures.

Electrodes S1 and S2 support different localized surface plasmon resonance (LSPR) modes (Fig. 1a), while S3 shows no plasmonic response. Specifically, S1 exhibits a plasmon band at around 657 nm and a broad absorption (857–926 nm), due to the excitation of surface plasmon waves in the Au NHs, acting as

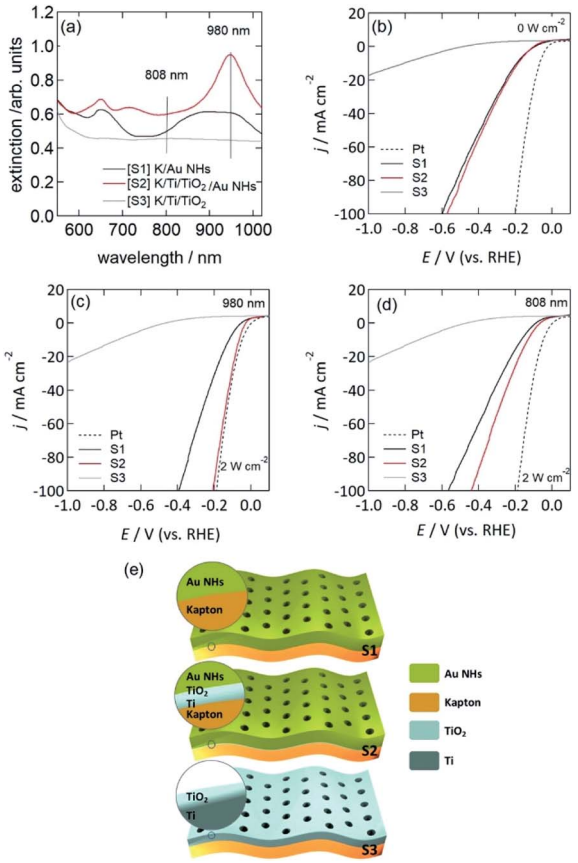

Fig. 1 Characteristics of the plasmonic electrodes. (a) UV/Vis absorption spectra of the different interfaces: S1: K/Au NHs (50 nm) (black), S2: K/Ti/TiO_2/Au NHs (50 nm) (red), S3: K/Ti/TiO_2 (30 nm) (grey), the vertical lines correspond to the two laser wavelengths used for HER investigation. (b) HER polarization curves of S1, S2, S3 and Pt in 0.1 M H_2SO_4 at a scan rate of 50 mV s^{-1} without illumination. (c) HER polarization curves of S1, S2, S3 and Pt under 980 nm light irradiation at 2 W cm^{-2} for 10 min. (d) HER polarization curves of S1, S2, S3 and Pt under 808 nm light irradiation at 2 W cm^{-2} for 10 min. All measurements were performed at room temperature. (e) Schematics of the three types of investigated systems.

two-dimensional diffraction gratings that convert incident photons into SP waves.[35] Note that the increase in absorption below 600 nm is due to the underlying Kapton substrate. The structure S2 displays, next to the plasmon band at 653 nm, an intense absorption band centered at around 980 nm with, however, a large half-wave width. This indicates a certain distribution of Au NH sizes with different LSPR maxima in the near infrared region.

The electrochemical behavior of the electrodes using ferrocenemethanol as the redox couple in aqueous solution reveals reversible voltammograms for S1 and S2 with a $\Delta E = 62$ mV. Structure S3 displays a quasi-reversible electron transfer behavior (Fig. S1b†) due to the presence of amorphous TiO_2, with poor electrical conductivity.[23]

2.2 Electrocatalytic activity towards the HER

The electrocatalytic activity of the samples towards the HER in acidic solution was investigated in a N_2-saturated 0.1 M H_2SO_4

Table 1 Overpotentials recorded for samples S1, S2 and S3 in 0.1 M H_2SO_4 with and without irradiation at 980 nm (2 W cm^{-2}) or 808 nm (2 W cm^{-2}) for 600 s in a thermostatted electrolyte (24 °C)

Substrate	Wavelength (nm)	η (V) [−10 mA cm^{-2}]	η (V) [−100 mA cm^{-2}]
S1	—	−0.212	−0.601
	980	−0.120	−0.395
	808	−0.201	−0.579
S2	—	−0.183	−0.598
	980	−0.045	−0.238
	808	−0.163	−0.431
S3	—	−0.533	—
	980	−0.462	—
	808	−0.462	—
Pt foil	—	−0.069	−0.201
	980	−0.043	−0.198
	808	−0.043	−0.198

electrolyte at room temperature. Their behaviour with and without light illumination is presented in Fig. 1. As shown in Fig. 1b, S3 (K/Ti/TiO_2) demonstrates poor HER activity.[23] In contrast, the surfaces with Au NHs exhibit electrocatalytic activity towards the HER with onset potentials shifting positively from −0.102 V (*vs.* RHE) (S1) to −0.098 V (*vs.* RHE) (S2). The small difference between S1 and S2 is most likely due to the difference in the charge transfer characteristics (see the ESI, Fig. S2†). For comparison, the onset potential of a Pt foil electrode under the same conditions is −0.025 V (*vs.* RHE).

Upon illumination with a laser at 980 nm at 2 W cm^{-2}, the HER activity of S1 and S2 is enhanced, while that of S3 remains almost unchanged (Fig. 1c). Interestingly, S2 outperforms the other surfaces and has a behavior close to that of a Pt sheet electrode under the same conditions. A comparison of the overpotentials η needed to achieve −10 and −100 mA cm^{-2} current densities (Table 1) suggests that the required potential energy for the HER is reduced on S2. With an overpotential of η = −0.045 V at −10 mA cm^{-2}, S2 approaches the thermodynamic potential of the HER (*i.e.* 0 V). It is also comparable to values attained on Pt foil electrodes under the same conditions, recording a current density of −10 mA cm^{-2} at η = −0.043 V under light illumination (dotted curves in Fig. 1). This change in η is most likely linked to the increase in the surface temperature of the Pt foil under light irradiation. Indeed, the solution temperature increased by about 5 °C under light irradiation. Note that the HER activity of S3 was not affected by light illumination.

In addition, the HER activities of S1, S2, S3 and Pt under illumination at 808 nm (2 W cm^{-2}) were assessed (Fig. 1d). The performance of S1 and S2 decreased compared to that observed under illumination at 980 nm, while that of S3 and Pt remained the same. The poor performance of S2 under illumination at 808 nm is related to the UV/Vis characteristics of this interface. Indeed, S2 exhibits an absorption minimum (Fig. 1a) at 808 nm. However, S2 displays an intense LSPR band at ∼980 nm, which is responsible for the strongly enhanced HER electrocatalytic activity under this wavelength illumination. These findings confirm that the HER enhancement of S2 is related to a plasmon-mediated effect. The same is true for S1.

Overall, the HER activity of S2 under 980 nm illumination is boosted compared to other plasmonic HER systems (Table 2). The results are competitive with the recently reported 3D nanoporous plasmonic heterostructures, formed by chemically dealloying a 700 nm thick Au–Ag alloy and post-coating with a monolayer of MoS_2 by chemical vapor deposition.[30] This electrocatalytic interface exhibits hydrogen production at an overpotential of −0.167 V (*vs.* RHE) under visible light illumination for −10 mA cm^{-2}. In this set up, the electrocatalyst is the MoS_2 monolayer and the HER performance was due to an efficient transfer of hot electrons from the gold nanopores to the monolayer MoS_2. In contrast to these plasmonic enhanced electrocatalytic systems, S2 formation is easy on the macroscale

Table 2 Comparison of S2 performance to literature values[c]

Interface	Conditions	η^a (V)	η^b (V)	Tafel slope (mV dec^{-1})	Ref.
Au@Ag/MoS_2	690 nm 25 mW cm^{-2}	−0.420	−0.55	155	36
MoS_2@Au	500 W UV/Vis lamp	−0.300	—	74	28
Amorphous MoS_2	No light	−0.180	−0.31	40	6
MoS_2@NPG	300 W Xe lamp 100 mW cm^{-2}	−0.167	−0.27	38	30
Au NRs on CoFe-MOF	808 nm	−0.135	−0.19	94	26
MoS_2@$Cu_{1.75}S$–Au	650 nm 0.1 W cm^{-2}	−0.120	—	39	27
N-doped porous carbon@Au	531 nm	−0.099	—	37	29
3D nanoporous metal phosphides	No light	−0.080	—	44	9
Nanoporous graphene with Ni dopants	_	−0.05	—	45	8
CoPS	No light	−0.048	—	56	7
Au NHs on Ti/TiO_2	**980 nm 2 W cm^{-2}**	**−0.045**	**−0.238**	**35**	**This work**

[a] −10 mA cm^{-2}. [b] −100 mA cm^{-2}. [c] MOF: metal–organic framework; NPG: annealed nanoporous plasmonic heterostructures.

 This journal is © The Royal Society of Chemistry 2020

(>10 cm^2) and the use of colloidal lithography makes the process highly reproducible.

As expected, the acceleration of electrochemical water reduction depends on the incident laser power density (Fig. 2). The onset HER potential decreases as the laser power increases from 500 mW cm^{-2} to 2 W cm^{-2}. At laser powers >1 W cm^{-2}, the polarization curves reach a pseudo steady state. Based on the polarization curves, the corresponding Tafel plots were estimated to evaluate the influence of light irradiation on the HER kinetics. The Tafel slopes without light activation are 144 mV dec^{-1} (S1) and 119 mV dec^{-1} (S2). Under 980 nm illumination at 2.0 W cm^{-2}, they decrease, respectively, to 104 mV dec^{-1} (S1) and 35 mV dec^{-1} (S2) (Fig. 2), indicating a good electrocatalytic activity, approaching the Pt value of 28 mV dec^{-1}. The reduction in the Tafel slope suggests that the surface adsorption of hydrogen increases. Under light irradiation, hydrogen bonds can thus be directly broken with desorption of hydrogen being the rate-limiting step.[11,29]

In addition, electrochemical impedance spectroscopy (EIS) measurements were carried out (Fig. S2†) to see if the charge transfer resistance (R_{ct}) changes occur under light illumination. In the case of the S2 electrode, the diameter of the semicircle in the Nyquist plot is slightly decreased under light illumination at 980 nm (2 W cm^{-2}) from 188 ± 6 to 127 ± 6 Ω cm^{-2}, revealing an enhancement of the electron transfer rate. For S1, the charge transfer resistance without light illumination is comparable to that of S2 (198 ± 11 Ω cm^{-2}). It decreases to 167 ± 12 Ω cm^{-2} upon light illumination with a 980 nm laser at 2 W cm^{-2} (Fig. S2†).

2.3 Mechanism

To understand the origin of the current enhancement, the HER reaction was performed at different solution temperatures up to 80 °C (Fig. S3†). The temperature corresponds to the surface temperature as determined with a thermocouple attached to the sample when immersed in 0.1 M H_2SO_4 and irradiated with a 980 nm laser at 2.0 W cm^{-2} for 10 min. We observe that the thermal heating effect upon the HER is weaker than the plasmonic effect.

To gain more evidence of the LSPR enhanced HER activity, the activation energy (E_a) of the HER (see the ESI†) was determined under light illumination at 980 nm and compared to that determined by heating the solution. The plots of ln j *vs.* $1/T$ revealed a linear relationship (Fig. S4†) in both cases. For S2, using the Arrhenius equation, the value of E_a under light irradiation was estimated to be 44 ± 5 kJ mol^{-1}, while in the dark it was 94 ± 1 kJ mol^{-1} (Fig. 3a). As observed by Wang *et al.* recently by investigating hydrogen evolution over metal–organic frameworks through plasmon-induced hot-electron injection,[26] the slopes of S1 and S2 of E_a *vs.* overpotential graph (Fig. 3a) under light are smaller compared to those in the dark. The decreased slope for S2 originates from direct hot-electron injection into the substrate due to plasmon activation. Plasmon-induced processes generate a significantly higher HER reactivity on S2 due to the formation of hot electrons.[13,26] This observation is adequately supported by the hot-electron-induced H_2 dissociation rate being increased by almost 2 orders of magnitude.[13]

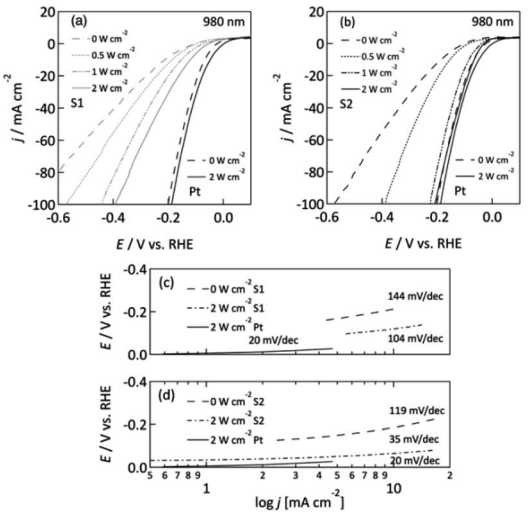

Fig. 2 Behavior of nanopatterned gold-based plasmonic electrodes towards the HER. (a) HER polarization curves of S1 illuminated at 980 nm at different laser power densities, scan rate = 50 mV s^{-1}. (b) HER polarization curves of S2 and Pt illuminated at 980 nm at different laser power densities, scan rate = 50 mV s^{-1}. (c and d) Tafel plots of the indicated electrodes derived from the initial stage of the HER polarization curves displayed in panels (a and b).

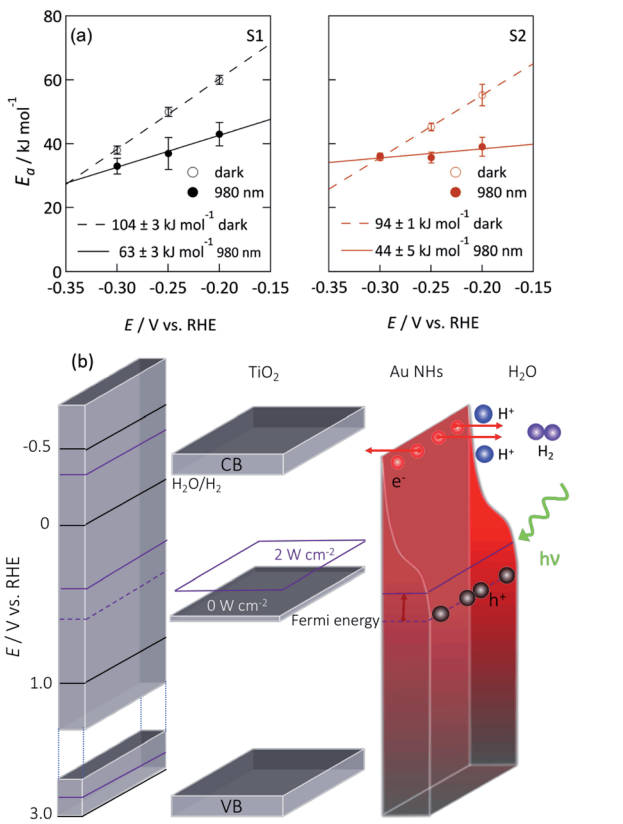

Fig. 3 Mechanistic considerations for the HER. (a) Activation energy as a function of overpotential upon 980 nm light irradiation (closed symbols) and in the dark (open symbols). (b) Schematic presentation of the mechanism involved in the HER on S2.

On the basis of the above results, the expected mechanism of the enhanced activity toward the HER under laser irradiation is the following: under laser excitation, surface plasmons are generated on the nanopatterned gold films forming electron–hole pairs (Fig. 3b). The generated hot electrons can then follow different pathways on S2:

(i) Recombination with the formed holes in the Au NH layer, being lost for electrocatalysis.

(ii) Direct electrochemical reduction of water to hydrogen gas on the Au NH surface.

(iii) Injection into the conduction band of the Ti/TiO_2 semiconductor adhesion layer followed by water reduction.

In the case of S1, where Au NHs are directly deposited on Kapton, no injection into the conduction band of the Ti/TiO_2 semiconductor adhesion layer occurs and only direct electrochemical reduction of water to hydrogen gas will occur. This results in a less efficient plasmon enhanced HER reaction. Indeed, for S1, the value of E_a under light irradiation is estimated to be 63 ± 3 kJ mol^{-1}, while in the dark it is 104 ± 3 kJ mol^{-1}. In this case, only direct electrochemical reduction of water occurs through the generation of hot electrons.

In S2, both direct electrochemical reduction of water and injection of hot electrons *via* the Mott–Schottky barrier into the thin Ti/TiO_2 layer occur, reflecting a low E_a under light irradiation of 44 ± 5 kJ mol^{-1}, assuming that the electron injection is faster than the electron–hole recombination process.

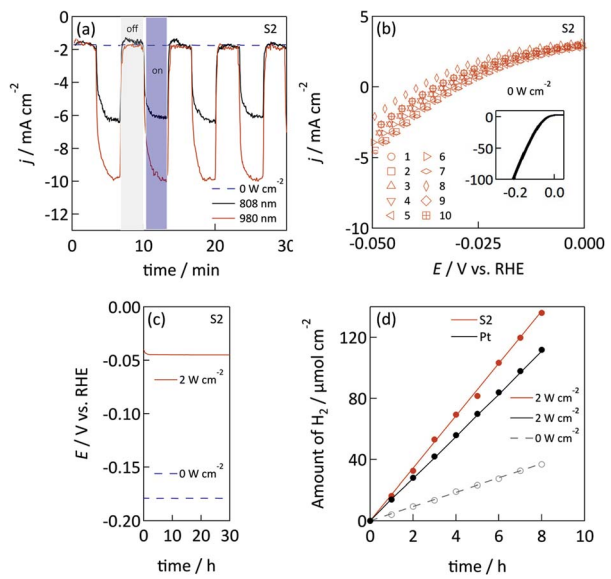

Fig. 4 Mechanistic considerations for the HER. (a) Current density–time curves under illumination at 980 nm (red), 808 nm (black) at 2 W cm^{-2} and with no illumination (dashed blue) for S2. (b) HER polarization curves of 10 S2 interfaces in 0.1 M H_2SO_4 at a scan rate of 50 mV s^{-1} in the dark. (c) HER stability tests of S2 at $j = -10$ mA cm^{-2} with (red, 2 W cm^{-2}) and without light (dashed blue) illumination by following the change of the overpotential with time. (d) H_2 production efficiency catalyzed by S2 at a potential of -0.040 V in 0.1 M H_2SO_4 with and without light irradiation. The theoretical efficiency (lines) was calculated according to the cumulative charge, assuming a 100% faradaic efficiency for H_2 production. The current density was $j = -10$ mA cm^{-2}. Data for Pt are shown as well (black symbols).

The fast generation and injection of hot electrons affect the current density profile abruptly upon laser irradiation, as illustrated in Fig. 4a, when S2 is biased at -0.048 V (*vs.* RHE). Interestingly, the surface temperature evolutions of S2 under 808 and 980 nm illumination at 2 W cm^{-2} are similar (Fig. S3†), pointing again to the key role of the hot electrons in the process rather than a solely thermally driven reaction.

2.4 Reproducibility

The HER activities are highly reproducible as seen in the curves recorded on 10 different S2 specimens (Fig. 4b). As stability is one of the key factors in determining the usefulness of an electrocatalyst, the long-term stability of the Au NH plasmonic catalyst was assessed using overpotential–time transient plots in an acid environment. Fig. 4c depicts the chronopotentiometric curves of S2 in 0.1 M H_2SO_4 aqueous solution at a current density $j = -10$ mA cm^{-2}. The overpotential–time measurements indicate an almost steady overpotential without any significant decay during 35 h of continuous HER, revealing excellent durability of the interface. The faradaic yields of H_2 production were in addition found to be quantitative within experimental errors (Fig. 4d). Up to 52 μmol cm^{-2} H_2 was formed after irradiation for 3 h, which represents a 4-fold enhancement compared to that of S2 without activation. The faradaic efficiency was determined as 97.2%.

3. Conclusion

In conclusion, nanoperforated gold structures coupled *via* Ti/TiO_2 adhesion layers to underlying Kapton substrates have been constructed as plasmonic electrocatalytic electrodes for catalysing the hydrogen evolution reaction in acidic medium. Upon light irradiation at 980 nm, the overpotential at a current density of -10 mA cm^{-2} decreases from -0.183 V to -0.045 V (*vs.* RHE). This HER activity of the plasmonic electrodes is comparable to that of Pt where under the same conditions an overpotential of -0.049 V (*vs.* RHE) was required. The interface sustains the hydrogen evolution reaction for several hours without surface poisoning or electrode degradation, as evidenced by the stable current density over time. Mechanistic investigations revealed that fast hot electron injection into the underlying Ti/TiO_2 layer is partially responsible for the enhanced HER activity. The good light trapping behaviour of the plasmonic electrodes might in addition allow direct electrochemical reduction of water due to a decrease in the HER activation energy under light irradiation. While TiO_2 is indeed one of the most promising semiconductors at present due to a thorough understanding of the role of the TiO_2 polymorph, any other semiconductor can be used for this application. Our findings reveal that nanopatterned gold electrodes, in the presence of metal oxide semiconductors, display a unique plasmonic enhanced HER.

4. Experimental

4.1 Fabrication of nanoperforated interfaces

Kapton substrates were modified with Au nanoholes according to our previous work,[33] with and without Ti adhesion layers. In short, a monolayer of 1000 nm polystyrene beads

 This journal is © The Royal Society of Chemistry 2020

(ThermoFisher Scientific) was deposited onto Kapton by self-assembly, followed by SF_6 and oxygen plasma etching for 8 min (gas flow 2 sccm and 30 sccm, respectively, at 10 mTorr chamber pressure) to reduce the particle size. The samples were then coated with metal or bi-metal layers at a constant deposition rate of 0.2 Å s^{-1} using physical vapor deposition. The beads on top of Kapton were removed by peeling the surface with Blue Low Tack tape (Semiconductor Equipment Corp.). The surfaces were washed with copious amounts of acetone and dried under nitrogen flow. The arrays display holes of 630 nm average size and a center-to-center spacing of 980 nm. Precisely, the samples were coated with either 50 nm Au (S1), ≈2 nm Ti followed by 50 nm Au (S2) or with only 30 nm Ti (S3).

4.2 Characterization

Scanning electron microscopy (SEM) images were obtained using an electron microscope, ULTRA 55 (Zeiss), equipped with a thermal field emission emitter and three different detectors (an EsB detector with a filter grid, a high efficiency in-lens SE detector, and an Everhart-Thornley secondary electron detector). The UV/Vis absorption spectra were recorded using a PerkinElmer Lambda UV-Vis 950 spectrophotometer.

4.3 Electrochemical experiments

Electrochemical measurements were performed with a Modu-Lab-MTS electrochemical test station (Solartron) in a standard three-electrode system with the plasmonic electrodes (or Pt) as the working electrode, a carbon plate as the counter electrode and an Ag/AgCl (3.5 M KCl) electrode as the reference electrode. The measured potentials were converted to that relative to the reversible hydrogen electrode (RHE) according to $E_{RHE} = E_{Ag/AgCl} + 0.059pH + E^{\circ}_{Ag/AgCl}$, with $E^{\circ}_{Ag/AgCl} = 0.1976$ V (25 °C).

Cyclic voltammetry (CV) and linear sweep voltammetry (LSV) measurements were performed in 0.1 M H_2SO_4 solution at a scan rate of 50 mV s^{-1}. Electrochemical impedance data were acquired over a frequency range of 100 kHz to 0.01 Hz.

The electrochemically active surface area (A) in the electrochemical cell was derived from the linear plot of the peak current as a function of the square root of the scan rate according to the equation $A = s/(268\,600 \times n^{3/2} \times D_f^{1/2} \times c_f)$, where n is the number of electrons transferred in the redox event ($n = 1$), D_f is the diffusion coefficient of ferrocenemethanol (7.5×10^{-6} cm^2 s^{-1}), c_f is the concentration of ferrocenemethanol (0.0001 mol cm^{-3}), and s is the slope of the linear fit to the data. The exposed area of the working electrode was 0.28 cm^2.

For plasmon-enhanced electrocatalysis, the electrode was illuminated with light from a continuous wave laser (980 and 808 nm, Gbox model, Fournier Medical Solution) with a laser power output between 0.5 and 2 W cm^{-2}. The temperature changes were captured using an infrared camera (Thermovision A40) and treated using ThermaCam Researcher Pro 2.9 software.

4.4 Faradaic efficiency

The faradaic efficiency (FE) of H_2 evolution was calculated by comparing the amount of volumetrically formed hydrogen to that calculated from potentiostatic cathodic electrolysis (assuming 100% FE). Assuming a one electron redox process, the number of moles (n) of H_2 formed during electrolysis can be calculated according to $n = Q/2F$, with F being the Faraday constant (96 485 C mol^{-1}) and Q the charge passed during the experiment. To determine the volume of H_2 formed, the outlet of the tightly closed electrolytic cell was connected to a tube that has been inserted into a beaker of 1 mL capacity filled with water. When H_2 gas is generated, the gas will flow into the tube and start displacing the water in the beaker.

Conflicts of interest

There are no conflicts to declare.

Acknowledgements

Financial support from the Centre National de la Recherche Scientifique (CNRS), the University of Lille and the Hauts-de-France region is acknowledged. P. L. thanks the Chinese government for the China Scholarship Council Award. S. M. is a Research Associate of the Belgian F.R.S. – FNRS and acknowledges financial support *via* the SELFPHON project.

References

1 J. A. Turner, *Science*, 2004, **305**, 972–974.
2 M. Fang, G. Dong, R. Wei and J. C. Ho, *Adv. Energy Mater.*, 2017, **7**, 1700559.
3 D. V. Esposito, S. T. Hunt, A. L. Stottlemyer, D. K. D. Dobson, B. E. McCandless, P. D. R. W. Birkmire and P. D. J. G. Chen, *Angew. Chem., Int. Ed.*, 2010, **49**, 9859–9862.
4 C. C. L. McCrory, S. Jung, I. M. Ferrer, S. M. Chatman, J. C. Peters and T. F. Jaramillo, *J. Am. Chem. Soc.*, 2015, **137**, 4347.
5 C. G. Morales-Guio, L.-A. Ster and X. Hu, *Chem. Soc. Rev.*, 2014, **43**, 6555–6569.
6 D. Merki, S. Fierro, H. Vrubek and X. Hu, *Chem. Sci.*, 2011, **1**, 1262–1267.
7 M. Caban-Acevedo, L. M. Stone, J. R. Schmidt, J. G. Thomas, Q. Ding, H.-C. Chang, M.-L. Tasi, J.-H. He and S. Jin, *Nat. Mater.*, 2015, **14**, 1245–1253.
8 H.-J. Qui, Y. Ito, W. Cong, Y. Tan, P. Liu, A. Hirata, T. Fujita, Z. Tang and M. Chen, *Angew. Chem., Int. Ed.*, 2015, **54**, 14031–14035.
9 Y. Tan, H. Wang, P. Liu, C. Cheng, F. Zhu, A. Hirata and M. Chen, *Adv. Mater.*, 2016, **28**, 2951.
10 H. Robatjazi, S. M. Bahauddin, C. Doiron and I. Thomann, *Nano Lett.*, 2015, **15**, 6155–6161.
11 Y. Shi, J. Wang, C. Wang, T.-T. Zhai, W. J. Bao, J.-J. Xu, X.-H. Xia and H.-Y. Chen, *J. Am. Chem. Soc.*, 2015, **137**, 7365–7370.
12 L. Yan, F. Wang and S. Meng, *ACS Nano*, 2016, **10**, 5452–5458.
13 S. Mukherjee, L. N. Zhou, A. M. Good man, N. Large, C. Ayala-Orozco, Y. Zhang, P. Nordlander and N. J. Halas, *J. Am. Chem. Soc.*, 2014, **136**, 64–67.

14 M. Murdoch, G. I. N. Waterhouse, M. A. Nadeem, J. B. Metson, M. A. Keane, R. F. Howe, J. Llorca and H. Idriss, *Nat. Chem.*, 2011, **3**, 489–492.
15 Y.-H. Chiu, S. B. Naghedeh, S. A. Lindley, T.-H. Lai, M.-Y. Kui, K.-D. Chang, J. Z. Zhang and Y.-J. Hsu, *Nano Energy*, 2019, **62**, 289–298.
16 Y.-H. Chui, T.-H. Lai, M.-Y. Kuo, P.-Y. Hsieh and Y.-J. Hsu, *APL Mater.*, 2019, **4**, 080901.
17 Y.-C. Pu, G. Wang, K.-D. Chang, Y. Ling, Y.-K. Lin, B. C. Fitzmorris, C.-M. Liu, X. Lu, Y. Tong, J. Z. Zhang, Y.-J. Hsu and Y. Li, *Nano Lett.*, 2013, **8**, 3817–3823.
18 J.-M. Li, C.-W. Tsao, M.-J. Fang, C.-C. Chen, C.-W. Liu and Y.-J. Hsu, *ACS Appl. Nano Mater.*, 2018, **1**, 12.
19 T.-H. Chiu, T.-H. Lai, M.-Y. Kuo, P.-Y. Hsieh and Y.-J. H. Hsu, *APL Mater.*, 2019, **7**, 080901.
20 Y. H. Jang, Y. J. Jang, S. Kim, L. N. Quan, K. Chung and D. H. Kim, *Chem. Rev.*, 2016, **116**, 14982.
21 S. Mukherjee, F. Libisch, N. Large, P. Neumann, L. V. Brown, J. Cheng, J. Britt Lassite, E. A. A. Carte, P. Nordlander and N. J. Halas, *Nano Lett.*, 2013, **13**, 240–247.
22 X. Li, S. Guo, C. Kan, J. Zhu, T. Tong, S. Ke, W. C. H. Choy and B. Wei, *Nano Energy*, 2016, **30**, 549–558.
23 B. Hou, L. Shen, H. Shi, R. Kapadia and S. B. Cronin, *Phys. Chem. Chem. Phys.*, 2017, **19**, 2877.
24 H. Cheng, M. Klapproth, A. Sagalchik, S. Li and A. Thomas, *J. Mater. Chem. A*, 2018, **6**, 2249.
25 Y. Shi, J. Wang, C. Wang, T.-T. Zhai, W.-J. Bao, J.-J. Xu, X.-H. Xia and H.-Y. Chen, *J. Am. Chem. Soc.*, 2015, **137**, 7365–7370.
26 S. S. Wang, L. Jiao, Y. Qian, W.-C. Hu, G.-Y. Xu, C. Wang and H.-L. Jiang, *Angew. Chem., Int. Ed.*, 2019, **58**, 10713–10717.
27 J. Cui, R. Jiang, W. Lu, S. Xu and L. Wang, *Small*, 2017, **13**, 1602235.
28 P. Siram, D.-S. Su, P. A. Periasamy, A. Manikandan, S.-W. Wang, H.-T. Chang, Y.-L. Chueh and T.-J. Yen, *Adv. Eng. Mater.*, 2018, **8**, 1801184.
29 H.-X. Zhang, Y. Li, M.-Y. Li, H. Zhang and J. Zhang, *Nanoscale*, 2018, **10**, 2236–2241.
30 Y. Zhang, J. Du, R. Luo, Z. Wang, Z. Wang, J. Han, P. Liu, T. Fujita, Q. Xue and M. Chen, *Nano Energy*, 2019, **58**, 552–559.
31 T. Wang, L. Liu, Z. Zhu, P. Papakostantinou, J. Hu, H. Liu and M. Li, *Energy Environ. Sci.*, 2013, **6**, 625–633.
32 T. Nait Saada, A. G. Marques da Silva, P. Subramanian, L. Pang, N. Adnane, B. Bjafari-Rouhani, V. Mishyn, D. Meziane, S. Melinte, G. Sandu, F. Dumeignil, S. Paul, R. Wojcieszak, R. Boukherroub and S. Szunerits, *J. Mater. Chem. A*, accepted.
33 C. Li, R. Ye, J. Bouckaert, A. Zurutuza, D. Drider, T. Dumych, S. Paryzhak, V. Vovk, R. O. Bilyy, S. Melinte, M. Li, R. Boukherroub and S. Szunerits, *ACS Appl. Mater. Interfaces*, 2017, **9**, 36665–36674.
34 J. Lausmaa, B. Kasemo and H. Mattsson, *Appl. Surf. Sci.*, 1990, **44**, 133–146.
35 K. Cheng, S. Wang, Z. Cui, Q. Li and S. Dai, *Appl. Phys. Lett.*, 2012, **100**, 253101.
36 Y. Kang, Y. Gong, Z. Hu, Z. Li, Z. Qiu, X. Zhu, P. M. Ajayan and Z. Fang, *Nanoscale*, 2015, **7**, 4482.

 This journal is © The Royal Society of Chemistry 2020